Chapter 6
Special Topics in Milling

If the facts don't fit the theory, change the facts.

- Albert Einstein

In Chapters 4 and 5 we analyzed the milling process for both stability and surface location error through frequency and time-domain approaches. Using frequency-domain analyses, we: 1) generated stability lobe diagrams that identify stable and unstable combinations of spindle speed and axial depth of cut; and 2) completed surface location error predictions over the same parameter space. We developed time-domain simulations for the circular tool path approximation that predict forces and displacements for square and ball endmills, including the effects of helical teeth geometries. We next extended the square endmill time-domain simulation to incorporate the actual cycloidal tool path and investigated both stability and surface location error for various cutting conditions. Finally, we compared stability and surface location error solutions between the frequency and time-domain analyses. In this chapter, we continue our investigation of milling by exploring the frequency content of stable and unstable milling signals and enhancing our time-domain simulations to include runout of the cutter teeth and variable teeth spacing. We then discuss low radial immersion milling and the corresponding stability behavior. We conclude the chapter with some comments regarding stability boundary uncertainty evaluation for the frequency-domain analyses.

6.1 Frequency Content of Milling Signals

Let's return to the average tooth angle analysis for milling stability from Section 4.3 [1]. The relationships used to determine the spindle speed dependent axial depth of cut limit, $b_{\lim}$, are repeated in Eqs. 6.1.1 through 6.1.3.

$$b_{\lim} = \frac{-1}{2K_s \mathrm{Re}[FRF_{orient}]N_t^*} \tag{6.1.1}$$

T.L. Schmitz, K.S. Smith, *Machining Dynamics*, DOI 10.1007/978-0-387-09645-2_6,

$$\frac{f_c}{\Omega N_t} = N + \frac{\varepsilon}{2\pi} \tag{6.1.2}$$

$$\varepsilon = 2\pi - 2\tan^{-1}\left(\frac{\mathrm{Re}[FRF_{orient}]}{\mathrm{Im}[FRF_{orient}]}\right) \tag{6.1.3}$$

As a reminder, we restate the variable definitions here:

- K_s, specific force – process dependent coefficient that relates the resultant cutting force to the uncut chip area;
- FRF_{orient}, oriented frequency response function – x and y direction frequency response functions, or FRFs, "weighted" by the direction orientation factors, which are determined from the two step projection of the cutting force (due to a tooth located at the average between the start and exit angles) first onto the x and y directions and then onto the average surface normal;
- N_t^*, average number of teeth in the cut – it is possible for multiple teeth to be engaged simultaneously and for the number of teeth in the cut to vary during a single revolution. The average value $N_t^* = \frac{\phi_e - \phi_s}{\frac{360}{N_t}}$ captures this behavior, where ϕ_e and ϕ_s are the exit and start angles (deg), respectively, and N_t is the number of teeth on the cutter;
- f_c, chatter frequency (Hz) – frequency at which self-excited vibrations will occur if the stability limit is exceeded;
- Ω, spindle speed (rev/s) – the rotating frequency of the spindle for milling;
- N, lobe number – $N = 0, 1, 2, \ldots$ indexed from right to left (higher to lower spindle speeds) in a stability lobe diagram; and
- ε, phase between the current and previous tooth vibrations (rad) – varies between π rad (180 deg) and 2π rad (360 deg), where $\varepsilon = 3\pi/2$ rad (270 deg) is the least favorable value.

We use Eqs. 6.1.1 through 6.1.3 to generate milling stability lobe diagrams for the average tooth angle approach by: 1) determining the oriented FRF and identifying the valid chatter frequency range(s), i.e., where the real part of FRF_{orient} is negative; 2) solving for ε over the valid frequency range(s); 3) finding the average number of teeth in the cut for the selected radial immersion; 4) calculating b_{lim} over the valid frequency range(s); 5) selecting an $N = 0, 1, 2, \ldots$ value (representing N waves of vibration between teeth) and calculating the associated spindle speeds over the valid frequency range(s); and 6) plotting Ω vs. b_{lim} for each N value. As we discussed previously, any (Ω, b) pair leads to stable or unstable behavior depending on whether it appears above or below the stability boundary, respectively.

In our discussions of both stability and surface location error, we showed spectra of the cutting force signals which included content not only at the tooth passing frequency, but also at multiple harmonics due to the "impulse train" nature of typical milling force profiles. The notable constant force exceptions

are: 1) slotting with an even number of teeth, where $N_t > 2$; and 2) particular axial depths of cut for helical square endmills which are determined from $b = \frac{d \cdot \phi_p}{2\tan(\gamma)}$, where d is the cutter diameter, $\phi_p = \frac{2\pi}{N_t}$ (rad) is the pitch angle, and γ is the helix angle. We expressed the tooth passing frequency as a function of the spindle speed (rpm) and number of teeth, $f_{tooth} = \frac{\Omega \cdot N_t}{60}$ (Hz). We can expect, then, that during stable cutting conditions we should observe content at f_{tooth} and integer multiples of this value.

"What about unstable cuts?", we may ask. We've already shown in Section 4.3, through our description of the average tooth angle approach, that each stability lobe can be described as a mapping of the oriented FRF onto the (Ω, b_{lim}) parameter space. See Fig. 4.3.4, for example, where the chatter frequency is scanned through its potential values to obtain the stability limit for each N value. We know, therefore, that the chatter frequency (should chatter occur) is not a fixed value. It depends on the spindle speed and occurs within the valid chatter frequency range from FRF_{orient}. We also found that increased axial depths of cut were available at the "best speeds" of $\Omega_{best} = \frac{f_n \cdot 60}{(N+1) \cdot N_t}$ (rpm), where f_n is expressed in Hz, although multiple vibration modes can lead to competing lobes and more complicated stability lobe diagrams. The purpose of this best speeds equation is to match the tooth passing frequency to the system natural frequency so that the tooth-to-tooth surface undulations are in phase, i.e., $\varepsilon = 360$ deg, and the force variation due to chip thickness modulation is minimized. Given this circumstantial information, we can expect that unstable cuts will exhibit content not only at f_{tooth} and its harmonics, but also some chatter frequency.

FOR INSTANCE Stable cuts sound different from those that chatter. Stable cuts generate sound at the tooth passing frequency, runout frequency (see Section 6.2), and multiples of these. For that reason, stable cuts sound "clean"; they produce "pure" tones. Unstable cuts, however, also emit sound at the chatter frequency, which is generally not a multiple of the tooth passing or runout frequencies. For this reason, unstable cuts sound "harsh" or "raspy". They exhibit a mixture of frequencies that are not harmonically related.

To explore the frequency content of milling signals in more detail, as well as how we might capitalize on this information, let's update the average tooth angle MATLAB® code we developed previously. In p_6_1_1_1.m, we'll add new figures to show the chatter and tooth passing frequencies, as well as the phase between surface undulations from one tooth to the next, as a function of spindle speed. We'll then see how we can use the chatter frequency for an unstable (Ω, b_{lim}) combination to select a new spindle speed and converge on the preferred $\varepsilon = 360$ deg phase relationship [2-3] in Ex. 6.1.1.

Example 6.1.1: Selecting new spindle speeds using the chatter frequency For simplicity, we'll consider the single degree of freedom model shown in Fig. 6.1.1. A single mode in the x (feed) direction is identified with $f_n = 800$ Hz, $k = 5 \times 10^6$ N/m, and $\zeta = 0.01$. We'll assume the y direction is rigid. The cutter has four teeth and the tool-material pair yields a specific force of $K_s = 2000\,\text{N/mm}^2$ and force angle of $\beta = 72$ deg for the 50% radial immersion up milling cut.

Our first task is to determine the directional orientation factor, μ_x. As detailed in Section 4.3, two steps are required to calculate this value. First, the force is projected onto the x direction. Second, this result is projected onto the average surface normal. As shown in Fig. 6.1.2, projection of the force onto the x direction gives $F_x = F\cos(\beta - 45)$. The projection of this result onto the average surface normal is $F_n = F_x\cos(45) = F\cos(\beta - 45)\cos(45)$. Using Eq. 4.3.5, we obtain $FRF_{orient} = \mu_x FRF_x = \cos(\beta - 45)\cos(45)FRF_x$. This result is displayed in Fig. 6.1.3 for the selected x direction dynamics. Figure 6.1.4 shows the valid chatter frequency range ($\text{Re}[FRF_{orient}] < 0$) for the oriented FRF (top) and corresponding $N = 0$ stability limit versus spindle speed in rev/s (bottom). Note the $\frac{1}{N_t}$ relationship between frequency and spindle speed from the top to bottom subplots. This mapping supports both the best speeds equation $\Omega_{best} = \frac{f_n}{(N+1)\cdot N_t} = \frac{800}{(0+1)\cdot 4} = 200\,\text{rev/s}$ and the worst speeds equation $\Omega_{worst} = \frac{f_c}{N_t}\cdot\frac{1}{N+\frac{\varepsilon}{2\pi}} = \frac{f_n(1+\zeta)}{4}\cdot\frac{1}{0+\frac{\frac{3\pi}{2}}{2\pi}} = \frac{800(1+0.01)}{4}\frac{1}{0+\frac{3}{4}} = 269.3\,\text{rev/s}$ since increased

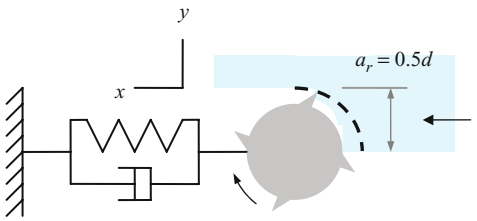

Fig. 6.1.1 50% radial immersion up milling model for Ex. 6.1.1

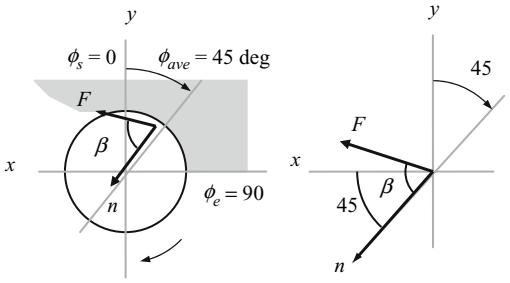

Fig. 6.1.2 Geometry for determining 50% radial immersion up milling directional orientation factor, μ_x

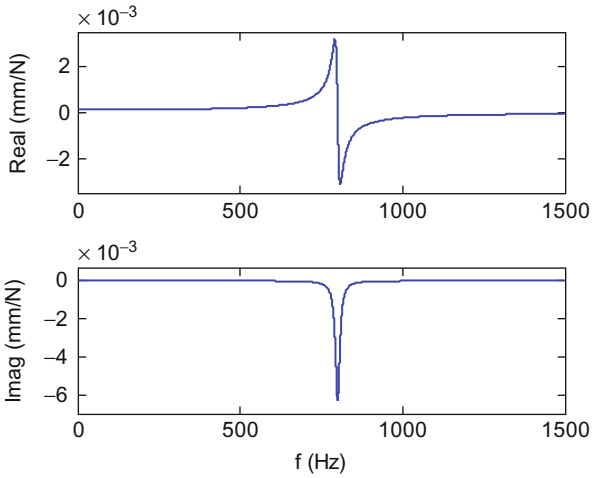

Fig. 6.1.3 Oriented frequency response function for Ex. 6.1.1

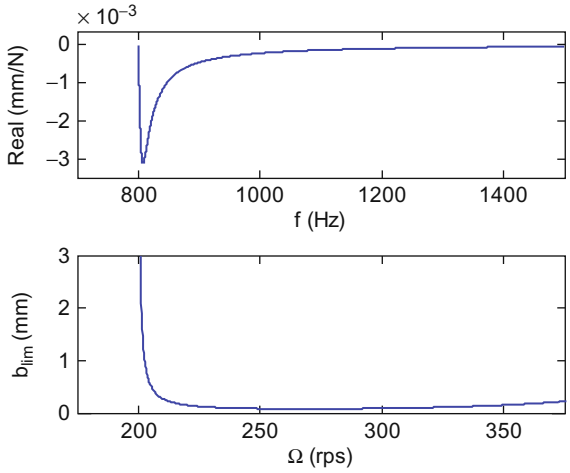

Fig. 6.1.4 Valid chatter frequency range for oriented FRF (top). Corresponding (Ω, b_{lim}) parameter space for $N = 0$ mapping (bottom)

axial depths are obtained near 200 rev/s and the minimum allowable depth, equal to the critical stability limit, occurs at 269.3 rev/s.

In Fig. 6.1.5, we have included the $N = 0$ to 4 stability lobes and converted the spindle speed to rpm in the top subplot. The bottom subplot shows the potential chatter frequencies (solid lines) and harmonics of the tooth passing frequency (dotted) as a function of spindle speed. The latter naturally grow linearly with spindle speed. The rightmost dotted line represents f_{tooth}, while

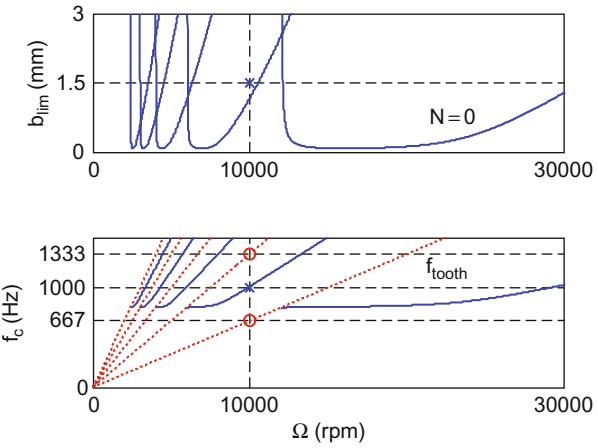

Fig. 6.1.5 (Top) Stability lobes for $N = 0$ to 4; the selected cutting condition of (10000 rpm, 1.5 mm) is indicated by the 'x'. (Bottom) The tooth passing frequencies (dotted lines) and chatter frequencies (solid) are shown as a function of spindle speed. The tooth passing frequency content at 667 Hz and 1333 Hz is identified by the circles, while the chatter frequency at 1000 Hz is located by the 'x'

subsequent dotted lines moving from right to left indicate increasing harmonics of $2f_{tooth}$ to $5f_{tooth}$. For this single degree of freedom case, the valid chatter frequencies begin at $f_n = 800$ Hz and then increase with spindle speed. This reiterates the behavior observed in Fig. 6.1.4, which shows the mapping from chatter frequency to spindle speed between the top and bottom subplots. Figure 6.1.5 also identifies selected points at 10000 rpm. We'll discuss these next.

Let's assume a cut was attempted at $\Omega = 10000$ rpm, $b = 1.5$ mm (suppose that we did not know if the cut would be stable or unstable). This cut is identified by the 'x' at $\Omega = 10000$ rpm and $b = 1.5$ mm in the top subplot. We would expect frequency content at $f_{tooth} = \frac{\Omega \cdot N_t}{60} = \frac{10000 \cdot 4}{60} = 667$ Hz, $2f_{tooth} = 2\frac{10000 \cdot 4}{60} = 1333$ Hz, and so on, if the cut was stable since only forced vibrations would be present. Circles in the bottom subplot indicate these frequencies within the plot's vertical limits. However, because the operating point (10000 rpm, 1.5 mm) is located in the unstable zone of the stability lobe diagram (top of Fig. 6.1.5), content will also be observed at 1000 Hz due to the self-excited vibration. This point is marked with an 'x' on the chatter frequency line in the bottom subplot. Note that this relationship between chatter frequency and spindle speed is defined in Eq. 6.1.2.

Returning to the best speeds equation, its purpose is to match the tooth passing frequency to the chatter frequency in order to drive the operating condition towards a tooth-to-tooth undulation phase relationship of $\varepsilon = 360$ deg. Given the chatter frequency of 1000 Hz identified in the bottom subplot of Fig. 6.1.5, we should select a new spindle speed of:

$$\Omega = \frac{f_c \cdot 60}{(N+1) \cdot N_t} = \frac{1000 \cdot 60}{(0+1) \cdot 4} = 15000 \text{ rpm}$$

for the $N = 0$ lobe and:

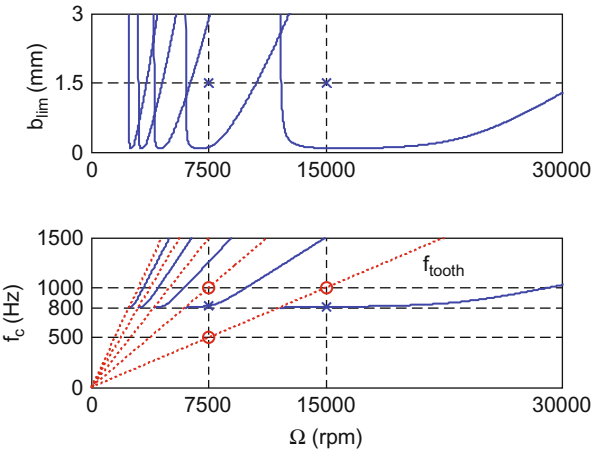

Fig. 6.1.6 (Top) A first spindle speed regulation scenario gives new speeds at 7500 rpm and 15000 rpm ($N = 1$ and 0 lobes, respectively) based on the 1000 Hz chatter frequency from Fig. 6.1.5. (Bottom) The new cutting conditions are also unstable and yield chatter frequencies of 818 Hz ($N = 1$) and 806 Hz ($N = 0$)

$$\Omega = \frac{f_c \cdot 60}{(N+1) \cdot N_t} = \frac{1000 \cdot 60}{(1+1) \cdot 4} = 7500 \text{ rpm}$$

for the $N = 1$ lobe. The tooth passing frequency for 15000 rpm is $f_{tooth} = \frac{15000 \cdot 4}{60} = 1000$ Hz, as expected. Similarly, the tooth passing frequency for 7500 rpm is $f_{tooth} = \frac{7500 \cdot 4}{60} = 500$ Hz and the second harmonic is 1000 Hz. The points are shown as the circles in the bottom subplot of Fig. 6.1.6. However, because the cuts at (15000 rpm, 1.5 mm) for the $N = 0$ lobe and (7500 rpm, 1.5 mm) for the $N = 1$ lobe are again unstable – see the top subplot of Fig. 6.1.6 – we will observe content at the corresponding chatter frequencies. These are 818 Hz and 806 Hz for the $N = 0$ and 1 lobe spindle speed adjustments, respectively. Each of these points is marked by an 'x' in the bottom subplot of Fig. 6.1.6. If we make a second spindle speed adjustment for the $N = 0$ lobe, for example, the new value is $\Omega = \frac{806 \cdot 60}{(0+1) \cdot 4} = 12090$ rpm. Figure 6.1.7 shows this final

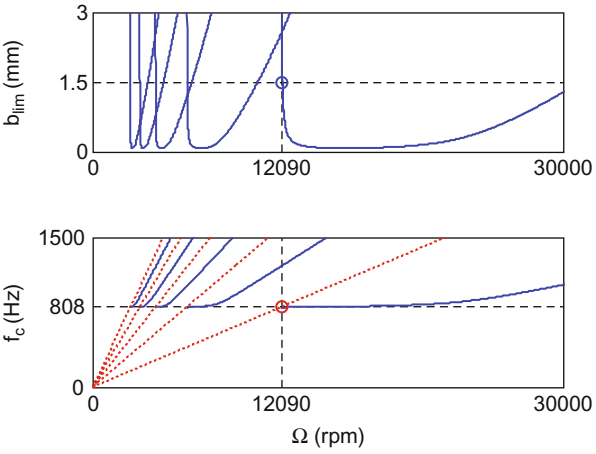

Fig. 6.1.7 (Top) Based on the 806 Hz chatter frequency at (15000 rpm, 1.5 mm) from Fig. 6.1.6, the new spindle speed is 12090 rpm. The new cut is identified by a circle and is stable. (Bottom) Because the cut is stable, the milling signal only includes content at $f_{tooth} = 806$ Hz (indicated by the circle) and integer harmonics, which occur outside the axis limits

regulation into the stable zone. On the other hand, the $N = 1$ lobe would yield a new spindle speed of $\Omega = \frac{818 \cdot 60}{(1+1) \cdot 4} = 6135$ rpm. Although this selection corresponds to the gap between the $N = 1$ and 2 lobes, the axial depth (gain) is still too high and the cut would again be unstable.

As we noted previously, we use the best speeds equation to converge on the $\varepsilon = 360$ deg phase relationship. Let's repeat the previous analysis but show the spindle speed versus ε relationship for the two regulations. Figure 6.1.8 displays the (Ω, b_{lim}) parameter space (top), as well as the (Ω, ε) relationship (bottom), again for the $N = 0$ to 4 lobes. We see that the tooth-to-tooth undulation phase relationship is initially 185 deg, or nearly directly out of phase, for the (10000 rpm, 1.5 mm) cutting condition.

As shown in Fig. 6.1.6, the first adjustment based on the 1000 Hz chatter frequency leads to new spindle speeds of 15000 rpm ($N = 0$ lobe) or 7500 rpm ($N = 1$). The corresponding (Ω, ε) diagram is provided in Fig. 6.1.9 (bottom). We see that the phase relationship between subsequent tooth passages is $\varepsilon = 229$ deg for $\Omega = 7500$ rpm and 290 for 15000 rpm. Both speeds are unstable (top). For the second spindle speed adjustment ($N = 0$ lobe), however, the $\Omega = \frac{806 \cdot 60}{(0+1) \cdot 4} = 12090$ rpm speed gives stable cutting conditions. The corresponding ε value is 357 deg, very near the "best" tooth-to-tooth undulation phase relationship of 360 deg. This case is shown in Fig. 6.1.10.

To conclude this example, let's describe potential sources of the required chatter frequency information, which we can use to converge on preferred spindle speeds for improvements in stable axial depths of cut. Essentially, any signal that is derived from the milling process is acceptable. However, the most common choices include force, displacement, and the audio signal emitted by the cutting process [3] due to acceptable signal-to-noise ratios in most instances. The cutting force is a natural option since it directly communicates not only the tooth passing frequency and harmonics, but also the chatter frequency for

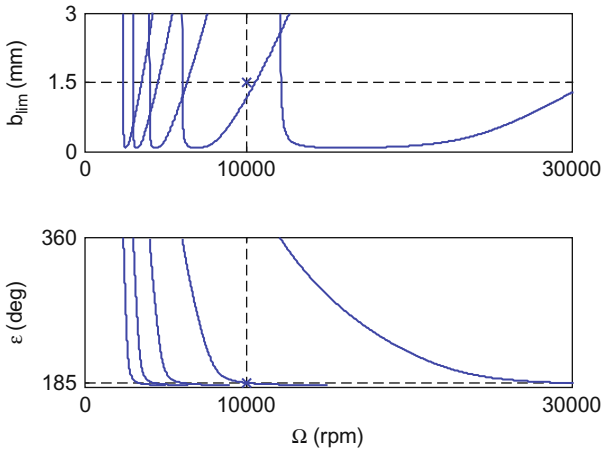

Fig. 6.1.8 (Top) Stability lobes for $N = 0$ to 4; the selected cutting condition of (10000 rpm, 1.5 mm) is indicated by the 'x'. (Bottom) The tooth-to-tooth undulation phase is shown as a function of spindle speed. The 185 deg phase for the unstable cut is identified by the 'x'

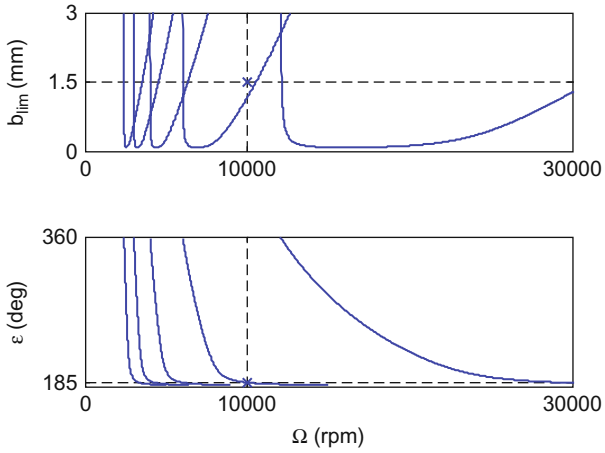

Fig. 6.1.9 (Top) The first spindle speed regulation gives new values at 7500 rpm and 15000 rpm ($N = 1$ and 0 lobes, respectively) based on the 1000 Hz chatter frequency from Fig. 6.1.5. (Bottom) The new cutting conditions are also unstable and yield ε values of 229 deg ($N = 1$ lobe) and 290 deg ($N = 0$)

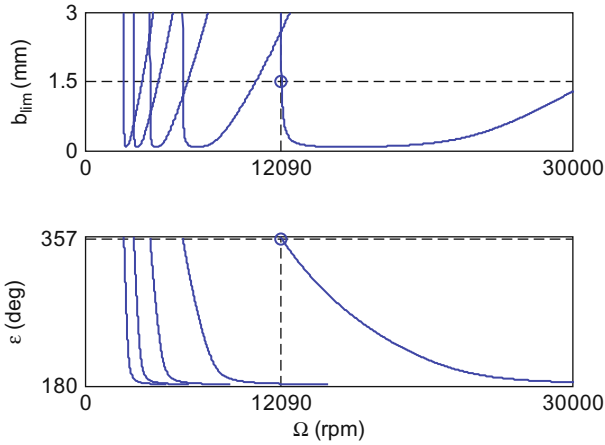

Fig. 6.1.10 (Top) For the 806 Hz chatter frequency observed in Fig. 6.1.6 for (15000 rpm, 1.5 mm), the new spindle speed is 12090 rpm. The stable cut is identified by the circle. (Bottom) The ε value is 357 deg for the stable cut

unstable conditions. The challenge, however, is obtaining this signal. Mounting a tabletop dynamometer between the workpiece and pallet/tombstone on the milling center is possible, but inherent drawbacks are: 1) the dynamometer influences the system dynamic response; 2) the dynamometer has a limited bandwidth so that content at higher frequencies may be corrupted by the

dynamometer response (see Section 4.7); 3) the cost is significant for commercially available cutting force dynamometers/amplifiers; and 4) this approach is not well suited to industrial applications. The information could also be obtained from the torque signal emitted by a spindle-based torque dynamometer [4]. However, the same difficulties apply. The tool displacement signal could also be used, but the tool-workpiece interface is notoriously difficult to instrument. Displacement can be recorded on the tool shank, but non-contact sensors will generally be affected by coolant, for example, and this approach is again not particularly well suited to shop floor conditions. The use of a microphone to record the cutting process audio signal offers a good compromise and has been implemented in a control system to sense and correct unstable cutting conditions using the techniques described in the previous paragraphs [5].

A natural challenge, regardless of the transduction scheme, is setting a limit on what magnitude of spurious frequency content (not at the tooth passing frequency or harmonics) constitutes chatter. This limit selection remains largely experience-based, although some efforts have been made toward automating the process of chatter identification. See [6-9], for example, which depend on the statistical distribution in the once-per-revolution (or once-per-tooth) sampled signal. The fundamental concept is that stable milling signals will repeat with the once-per-revolution/tooth sampling because the vibration is synchronous with the force. For self-excited vibrations, on the other hand, vibration occurs at the system natural frequency (corresponding to the most flexible mode) which is incommensurate[1] with the forcing frequency in general. When the unstable milling signal is sampled at once-per-revolution/tooth, therefore, it will not repeat [10]. The statistical variation in the unstable (and asynchronous) sampled signal will be larger than for the stable sampled signal.

IN A NUTSHELL It is surprising that, given the complexity of milling (including the tooth passing frequency content and system dynamics), there exists such a simple strategy for directing unstable cuts into stable zones. The basic steps are: 1) record the frequency content of the cutting signal; 2) ignore any frequency components caused by the teeth passing or runout; 3) if there is a significant frequency content remaining, define it as chatter (this is the "chatter detector"); and 4) choose a new spindle speed so that the tooth passing frequency is equal to the detected chatter frequency. This approach identifies a stable speed if one is available at the selected axial and radial depths of cut.

[1] In other words, the ratio of the natural frequency to forcing frequency cannot be expressed as a ratio of whole numbers [60].

Example 6.1.2: Selecting new spindle speeds in the presence of competing lobes To continue with our study of milling frequency content in the presence of chatter, let's consider a slightly more complicated dynamic system with two modes modeled in both the x and y directions. The symmetric modal dynamics are described by: $f_{n1} = 800$ Hz, $k_1 = 5 \times 10^6$ N/m, and $\zeta_1 = 0.01$ (first mode); and $f_{n2} = 900$ Hz, $k_2 = 9 \times 10^6$ N/m, and $\zeta_2 = 0.02$ (second mode). We'll consider the 25% radial immersion up milling cut depicted in Fig. 6.1.11, which is completed using a four tooth cutter in a tool-material pair that exhibits a specific force of $K_s = 700$ N/mm^2 and force angle of $\beta = 66$ deg.

The exit angle is calculated using Eq. 4.1.4:

$$\phi_e = \cos^{-1}\left(\frac{r - \frac{r}{2}}{r}\right) = \cos^{-1}(0.5) = 60\,\text{deg}$$

and the start angle for the up milling cut is zero. To find μ_x, we first project F onto the x direction to obtain $F_x = F\cos(\beta - 60)$, where β is given in deg. The projection of this result onto the average surface normal, which occurs at the angle $\phi_{ave} = \frac{0+60}{2} = 30\,\text{deg}$, is $F_n = F_x\cos(60) = F\cos(\beta - 60)\cos(60)$. For μ_y, projection onto the y direction gives $F_y = F\cos(150 - \beta)$. The projection of this result onto the average surface normal is $F_n = F_y\cos(150) = F\cos(150 - \beta)\cos(150)$. The directional orientation factors are therefore $\mu_x = \cos(\beta - 60)\cos(60)$ and $\mu_y = \cos(150 - \beta)\cos(150)$.

This oriented FRF is shown in Fig. 6.1.13 for the symmetric two mode dynamics. The top subplot in Fig. 6.1.14 displays the negative real part of FRF_{orient} so that the two valid chatter frequency ranges may be identified, while the bottom subplot provides the $N = 0$ stability limit versus spindle speed in rev/s (bottom). The two sections correspond to the two chatter frequency ranges and the overall stability limit is the lowest point from the pair at

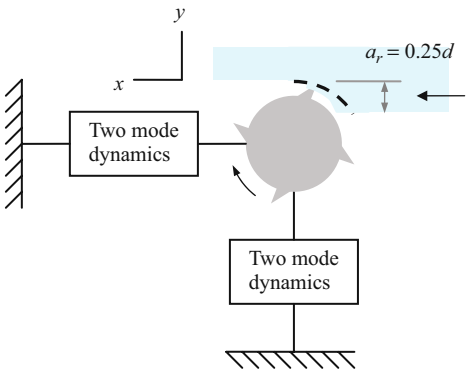

Fig. 6.1.11 25% radial immersion up milling model for Ex. 6.1.2

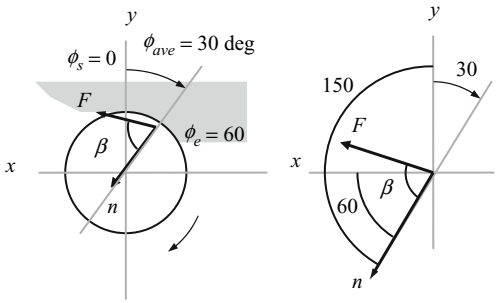

Fig. 6.1.12 Geometry for determining 25% radial immersion up milling directional orientation factors

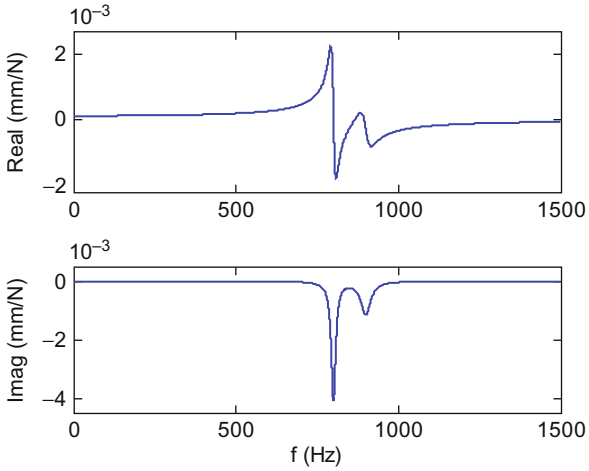

Fig. 6.1.13 Oriented frequency response function for Ex. 6.1.2

each spindle speed where they overlap. You may recall that this situation is referred to as "competing" lobes, as described in Section 4.3.

If the cutting conditions are initially selected to be 20000 rpm (let's say this is the maximum available spindle speed) with an axial depth of 2 mm, chatter would be observed. Similar to the previous example, however, we know that if we can obtain the chatter frequency from an appropriate transducer then we can use this information to select a new spindle speed. In Fig. 6.1.15, the unstable cutting conditions are identified by an 'x' in the top subplot. In the bottom subplot, we see that the chatter frequency for 20000 rpm is 919 Hz; we also know that the tooth passing frequency is $f_{tooth} = \frac{20000 \cdot 4}{60} = 1333$ Hz. These frequencies are marked with an 'x' and circle, respectively. Similar to the competing lobes, the chatter frequency curve for each N value has two distinct

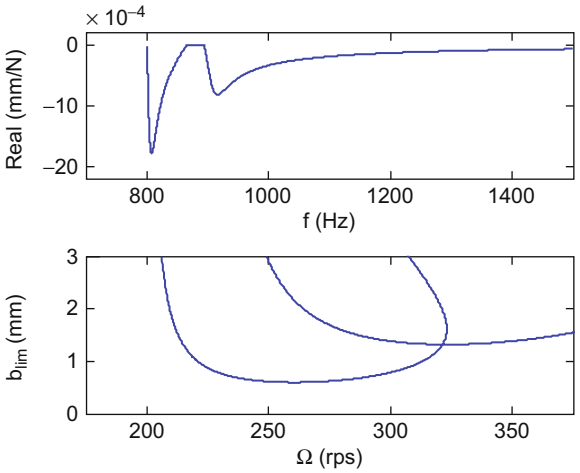

Fig. 6.1.14 Valid chatter frequency range for oriented FRF (top). Corresponding (Ω, b_{lim}) parameter space for $N = 0$ mapping (bottom). Competing lobes are seen due to the two valid chatter frequency ranges

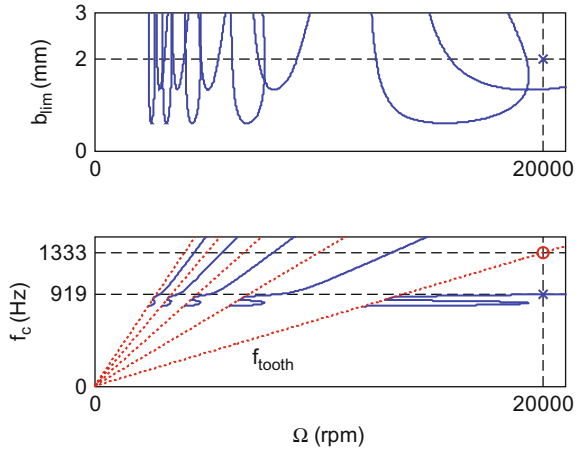

Fig. 6.1.15 (Top) Stability lobes for $N = 0$ to 4; the selected cutting condition of (20000 rpm, 2 mm) is indicated by the 'x'. (Bottom) The tooth passing frequency content at 1333 Hz is identified by the circle, while the chatter frequency at 919 Hz is marked by the 'x'

sections. Because the stability limit for the second section of the $N = 0$ lobe is exceeded in this instance, the chatter frequency also occurs on the second section of the chatter frequency curve for $N = 0$.

Based on our previous discussions, we know that the Fourier transform of the time-domain milling signal for the unstable cut will contain content at f_c, as well as f_{tooth} and its harmonics. The corresponding phase relationship for

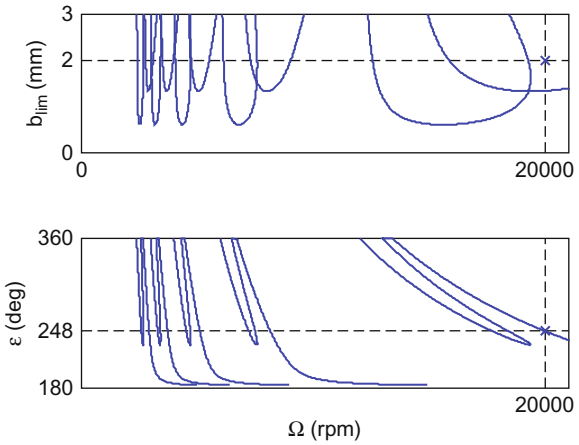

Fig. 6.1.16 (Top) Stability lobes for $N = 0$ to 4; the unstable cutting condition of (20000 rpm, 2 mm) is indicated by the 'x'. (Bottom) The tooth-to-tooth undulation phase of 248 deg for the unstable cut is identified by the 'x'

surface undulations between subsequent teeth is provided in Fig. 6.1.16. From the bottom subplot, we see that $\varepsilon = 248$ deg for the initial, unstable milling conditions. Further, this value is obtained from the second section of the undulation phase curve for $N = 0$.

Based on the 919 Hz chatter frequency from Fig. 6.1.15, the new spindle speed for $N = 0$ is $\Omega = \frac{919 \cdot 60}{(0+1) \cdot 4} = 13785$ rpm. The updated operating condition is shown in the top subplot of Fig. 6.1.17, where we see that the cut is again unstable. We also observe that this initial regulation moved the spindle speed to the left of the second competing lobe because chatter occurred in this section from the first cutting condition. The corresponding chatter frequency

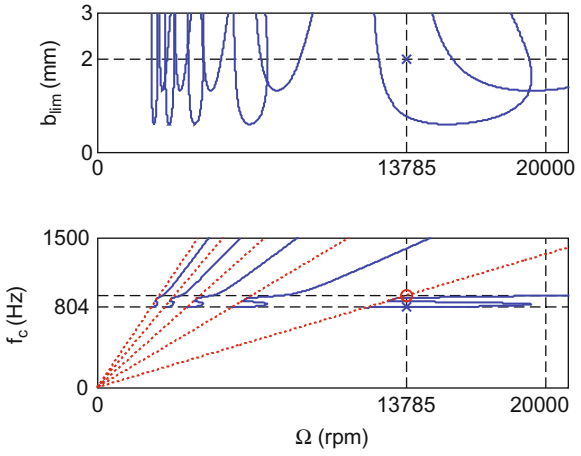

Fig. 6.1.17 (Top) The first spindle speed regulation gives a new speed at 13785 rpm ($N = 0$) based on the 919 Hz chatter frequency from Fig. 6.1.15. The new cutting condition is also unstable. (Bottom) The new cutting condition is also unstable and gives a chatter frequency of 804 Hz ($N = 1$); this value is located by the 'x'. The tooth passing frequency at 919 Hz is identified with a circle

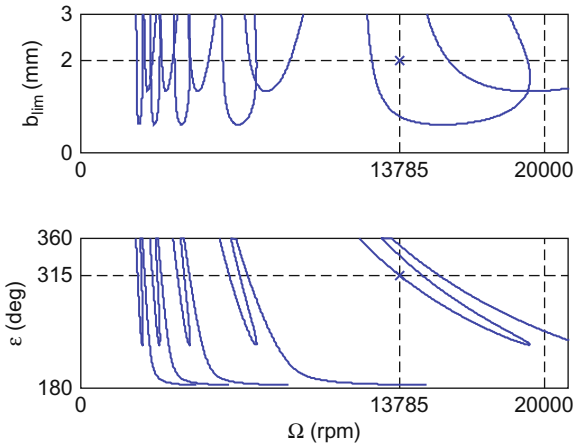

Fig. 6.1.18 (Top) The first spindle speed regulation gives a new speed at 13785 rpm ($N = 0$). This new condition is again unstable. (Bottom) The undulation phase is 315 deg for the new unstable cutting condition, (13785 rpm, 2 mm)

is 804 Hz. As seen in the bottom subplot, this chatter frequency is obtained from the lower portion of the first section of the curve because the stability limit imposed by the first competing lobe is exceeded to the left of the reversal in speed direction at 19384 rpm. The undulation phase is determined from Fig. 6.1.18. We see that $\varepsilon = 315$ deg and the value is again obtained from the first section of the undulation phase curve following the same logic as for the chatter frequency.

A second regulation to $\Omega = \frac{804 \cdot 60}{(0+1) \cdot 4} = 12060$ rpm provides a stable cutting condition, however. The new spindle speed is located to the left of the first competing lobe for $N = 0$, where increases in the stable axial depth may be obtained. The new operating point and corresponding tooth passing frequency (804 Hz) are shown in Fig. 6.1.19. The undulation phase is displayed in Fig. 6.1.20 (358 deg). Figures 6.1.13 through 6.1.20 were obtained using p_6_1_2_1.m, which is included on the companion CD.

6.2 Runout

One complication that we did not address in the previous section is that content other than the tooth passing frequency, its harmonics, and the chatter frequency may be present in the milling signal spectrum (i.e., the magnitude of the Fourier transformed time-domain signal). Even in the absence of external noise sources, such as pumps on the machine tool and other equipment on the shop floor, for example, runout (or eccentricity) leads to content in the milling

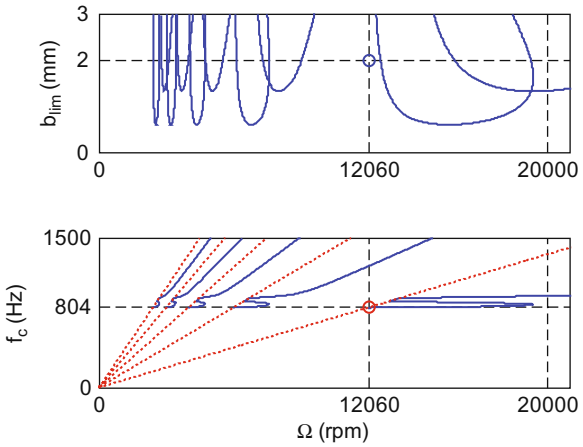

Fig. 6.1.19 (Top) The second spindle speed regulation gives a new stable speed of 12060 rpm ($N = 0$) based on the 804 Hz chatter frequency from Fig. 6.1.17. (Bottom) The tooth passing frequency for the stable cut is 804 Hz (circle)

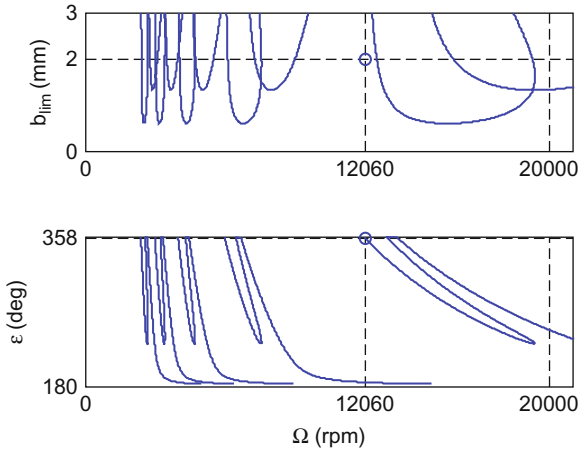

Fig. 6.1.20 (Top) The second spindle speed regulation provides a new stable speed of 12060 rpm ($N = 0$). (Bottom) The undulation phase is 358 deg for the stable cutting condition, (12060 rpm, 2 mm)

signal which is synchronous with spindle speed. Here we include the following possibilities under the generic heading of runout:

- axis of rotation errors of the spindle, including radial excursions of the spindle centerline during rotation [11-13];
- an offset between the holder centerline and spindle axis of rotation;
- an offset between the tool centerline and holder centerline; and

- radii variation between cutter teeth due to imperfect grinding for a solid tool or errors in the cutting edge placement for inserted cutters.

For demonstration purposes, let's focus on variation in the teeth radii as shown in Fig. 6.2.1. Naturally, the associated variation in chip thickness due to the "big tooth" is synchronous with spindle rotation. This generates frequency content at the runout frequency, $f_{ro} = \frac{\Omega}{60} = \frac{f_{tooth}}{N_t}$ (Hz), where Ω is expressed in rpm and f_{tooth} in Hz. We also observe content at the higher harmonics $2f_{ro}$, $3f_{ro}$, ... in general.

Example 6.2.1: Frequency content in the presence of runout If we return to Ex. 6.1.1 and plot the chatter frequency, tooth passing frequency and harmonics, and runout frequency with its first few harmonics (using p_6_2_1_1.m), we see that the third runout harmonic, $3f_{ro}$, intersects the chatter frequency curve (solid line). We also observe that $4f_{ro}$ (dot-dashed line) exactly overlaps f_{tooth} (dotted line). The latter is expected because $N_t = 4$. According to Fig. 6.2.2 (bottom subplot), we cannot discern between a potential chatter frequency and the third runout harmonic at 808 Hz, as indicated by the diamond. This is an important issue because one strategy to aid in isolating the chatter frequency for unstable cuts is applying a comb filter, i.e., a frequency-domain filter that passes all content except at selected equally spaced frequencies, to reject the tooth passing frequency and its harmonics [3-4]. The same technique cannot be applied to remove runout content if it coincides with possible chatter frequencies [14].

Let's use Eq. 6.1.2 to determine when this intersection between the chatter frequency and runout harmonics may occur. Restating this equation, we have that $\frac{f_c}{\Omega N_t} = N + \frac{\varepsilon}{2\pi}$. We also have the relationship $nf_{ro} = n\Omega$ where $n = 1, 2, 3, \ldots$ and Ω is expressed in rev/s in both instances. We are looking for instances when the chatter frequency is equal to a runout harmonic, or $f_c = nf_{ro} = n\Omega$. Substituting for f_c from Eq. 6.1.2 and solving for n, we obtain:

$$n = N_t\left(N + \frac{\varepsilon}{2\pi}\right). \tag{6.2.1}$$

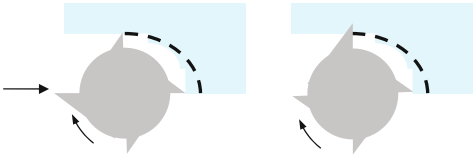

Fig. 6.2.1 Example of runout from a deviation in the radius from tooth to tooth in a solid endmill. (Left) A tooth with the nominal radius is entering the up milling cut where the chip thickness is zero according to the circular tool path approximation. (Right) The "big tooth" has a non-zero chip thickness for the same cutter angle

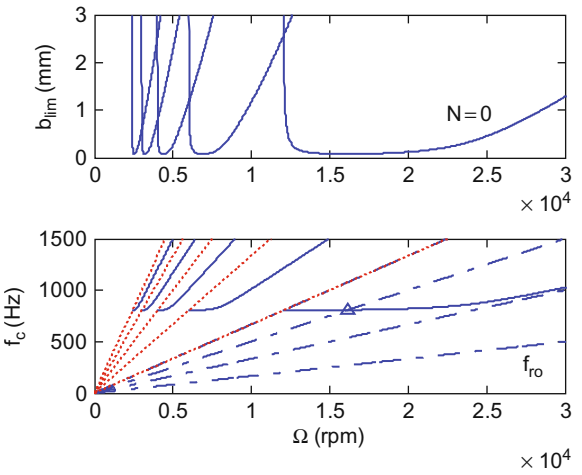

Fig. 6.2.2 An intersection between the third runout harmonic and the chatter frequency curve is seen at 808 Hz (marked by the diamond). This impedes our ability to identify potential chatter frequencies in the milling signal spectrum

Because $\pi < \varepsilon < 2\pi$ rad (see Fig. 3.3.2, for example), only particular integer n values yield acceptable ε values for a selected number of teeth and lobe number. We'll explore this in Ex. 6.2.2.

Example 6.2.2: Identifying intersections between runout harmonics and chatter frequencies Consider a four tooth cutter that exhibits runout. For the $N = 0$ lobe, we have that $n = 4\left(\frac{\varepsilon}{2\pi}\right)$ from Eq. 6.2.1. If $n = 1$, we obtain $\varepsilon = \frac{\pi}{2}$; therefore, no intersection is possible because this is not an acceptable ε value. For $n = 2$, we find that $\varepsilon = \pi$. However, because $\varepsilon \to \pi$ only as $f_c \to \infty$, this asymptotic approach is not practically important. For $n = 3$, on the other hand, $\varepsilon = \frac{3\pi}{2}$ and an intersection is possible as shown in Fig. 6.2.2. We also know from Section 4.3 that this is the least favorable tooth-to-tooth undulation phase relationship (for a single degree of freedom system). Note that if we know ε and f_c, then we can calculate the corresponding spindle speed for a selected lobe number by rearranging Eq. 6.1.2. Specifically, we compute:

$$\Omega = \frac{f_c}{\left(N + \frac{\varepsilon}{2\pi}\right)N_t} = \frac{808}{\left(0 + \frac{\frac{3\pi}{2}}{2\pi}\right)4} = 269.3\,\text{rev/s} = 16160\,\text{rpm}.$$

When $n = 4$, we have an overlap with f_{tooth} and intersection is only possible for $\varepsilon = 2\pi$, which represents the most favorable undulation phase.

Runout in milling affects the instantaneous chip thickness as demonstrated in Fig. 6.2.1. Therefore, the force is also influenced and, subsequently, the vibration. Well-known outcomes include premature cutting

edge failure and increased machined surface roughness. We can investigate these effects using updated versions of our time-domain simulations.

6.5.1 Simulation Modification

Incorporating the effects of runout in the cutter teeth, as depicted in Fig. 6.2.1, is straightforward. We'll first consider the circular tool path time-domain simulation for helical square endmills introduced in Section 4.5. Including runout requires that we modify the chip thickness, `h`, calculation to be:

```
h = ft*sin(phia*pi/180) + surf(cnt4, phi_counter) - n +
     RO(cnt3);
```

where `ft` is the feed per tooth, `phia` is the tooth angle for the current tooth and axial slice, `surf` is the array the contains the surface position for the previous tooth at each axial slice, `n` is the current vibration along the instantaneous surface normal direction, and `RO` is the vector that contains the tooth-to-tooth runout values. To establish a convention for the simulation and match general measurement procedures, we'll normalize the `RO` vector entries to the largest tooth radii (i.e., we'll set the dial indicator to zero at the largest tooth and measure the deviation in radii, if any, for the other teeth). This means that one `RO` entry will be zero and all other values will be zero (for no runout) or less than zero if runout is present. Naturally, the number of entries in this vector is N_t.

In addition to changing the chip thickness calculation, the `surf` array updating must include the runout effect. Specifically, we use the following line when the computed chip thickness is greater then zero (i.e., the current tooth is cutting).

```
surf(cnt4, phi_counter) = n - RO(cnt3);
```

This approach neglects variation in runout along the tool axis, which is clearly possible for actual cutters. To include axial dependence, the `RO` vector could be redefined as an array with a column for each tooth and a row for each axial slice, for example. We leave this activity as an exercise. As an example of the effect of runout, let's show the force profile for the helical endmill described in Ex. 4.5.1 together with the force variation in the presence of tooth-to-tooth runout.

Example 6.2.3: Comparison of forces with and without runout In this example, we compare the cutting forces produced by helical endmills with and without runout. We'll consider a 30% radial immersion up milling cut (zero start angle and 66.4 deg exit angle). There are two identical modes in both the x and y directions. The modal parameters are: $f_{n1} = 800$ Hz, $k_{q1} = 2 \times 10^7$ N/m, and $\zeta_{q1} = 0.05$; and $f_{n2} = 1000$ Hz, $k_{q2} = 1.5 \times 10^7$ N/m, and $\zeta_{q2} = 0.03$. The workpiece material is an aluminum alloy and it is machined with a four tooth, 19 mm diameter, 45 deg helix square endmill using a feed per tooth of 0.15 mm/tooth. The cutting force coefficients are $k_t = 520$ N/mm^2 and $k_n = 300$ N/mm^2. The corresponding stability diagram is shown in Fig. 4.5.5. The resultant

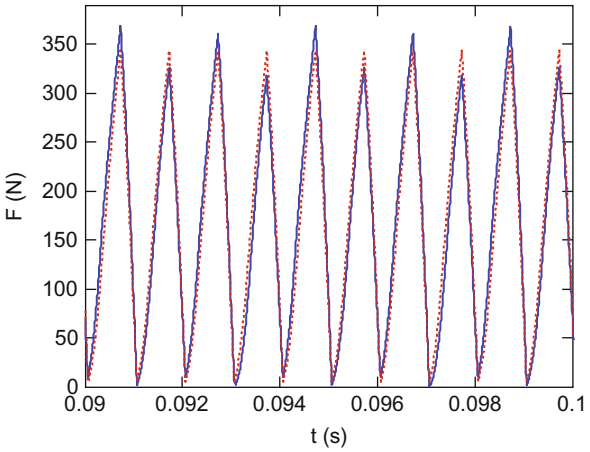

Fig. 6.2.3 Comparison of the resultant cutting force without runout (dotted line) and with runout (solid line) for the circular tool path simulation

cutting force for an axial depth of 5 mm at a spindle speed of 15000 rpm with no runout is shown as the dotted line in Fig. 6.2.3. The force with runout, `RO = [ 0 -10 0 -15]` μm, is shown as the solid line. At $t = 0.0977$ s, the runout force is smaller by 25.5 N (7.4% decrease from the nominal force). At $t = 0.0947$ s, the runout force is larger by 25.1 N (7.3% increase). This behavior matches the "big-little" teeth profile described by the selected runout values. Figure 6.2.3 was produced using the MATLAB® program p_6_2_3_1.m.

Let's now consider the cycloidal tool path simulation. We define the tooth dependent runout values in vector form, again using the same convention (normalized to a maximum value of zero). The only other changes to the program described in Section 5.3 are updating the radius with the runout values, `r = d/2 + RO`, and indexing `r` by the appropriate `Nt` counter each time it appears [15].

Example 6.2.4: Comparison of cycloidal and circular tool path results In this example, we compare the cutting forces for the cycloidal tool path simulation (p_6_2_4_1.m) to those observed in Ex. 6.2.3. The conditions are identical. The results with and without runout, `RO = [ 0 -10 0 15]` μm, are shown in Fig. 6.2.4. We see that the force levels are similar to those seen in Fig. 6.2.3. Perhaps more interesting, however, is a comparison of the machined surface profiles predicted by the cycloidal simulation. Figure 6.2.5 shows the surface without runout; the corresponding roughness average is 0.08 μm. When including runout, the roughness average increases to 0.66 μm (greater than eight times larger) as seen in Fig. 6.2.6. Note that the surface location error at the tool's free end is essentially unaffected: 87.4 μm overcut without runout and 86.1 μm when including runout effects. Additional information regarding the influence of runout on machining behavior can be found in [15-34]. In [15], for example,

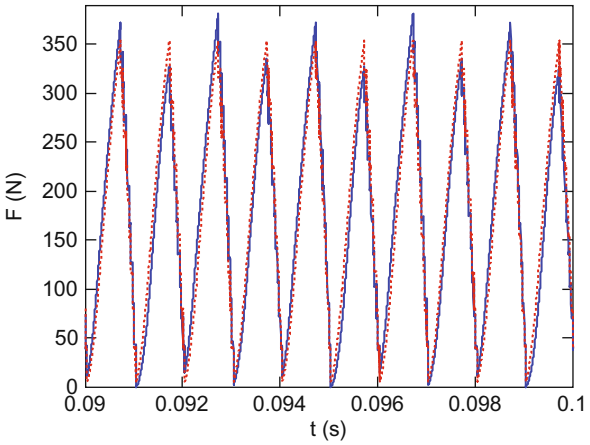

Fig. 6.2.4 Comparison of the resultant cutting force without runout (dotted line) and with runout (solid line) for the cycloidal simulation

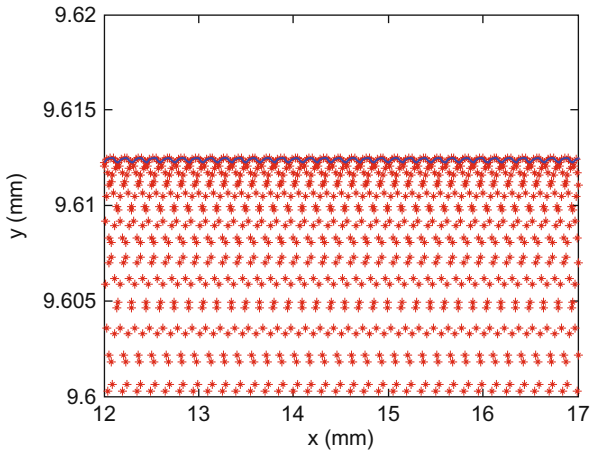

Fig. 6.2.5 Machined surface profile for Ex. 6.2.4 with no runout. The '*' symbols indicate the simulated cutting edge locations. The surface is shown by the solid line; it is defined using the "bubble up" algorithm described in Section 5.3. Note that the remaining material is located above the line for the up milling cut

the influences of runout, feed per tooth, and teeth spacing on surface roughness, surface location error, and stability are explored.

6.3 Variable Teeth Spacing

In all our previous stability analyses, we have assumed that the teeth are equally spaced around the cutter periphery (i.e., constant teeth pitch). It is of course also possible to place the teeth with unequal, or non-proportional, spacing.

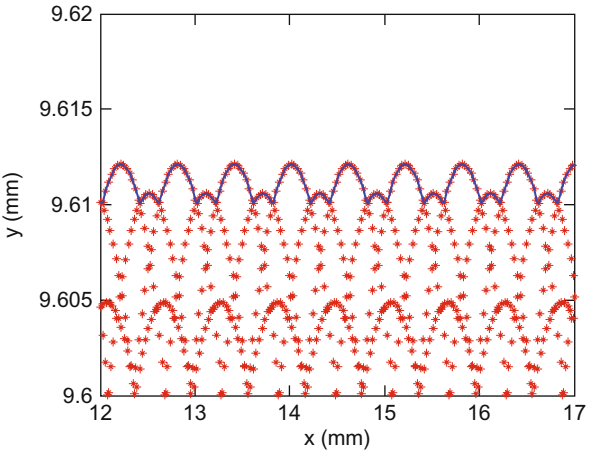

Fig. 6.2.6 Machined surface profile for Ex. 6.2.5 with runout. The roughness average is approximately eight times higher than the surface in Fig. 6.2.5

Several researchers have implemented variable teeth spacing to interrupt regeneration of surface waviness (caused by tool vibrations) and, therefore, modify stability behavior [35–43]. Although we could argue that determining the stability lobe diagram and using it to select cutting parameters is a valid approach, the use of variable teeth spacing can be applied in situations where it is inconvenient to adjust the spindle speed, such as a transfer line, or the larger stable lobes available at higher spindle speeds are inaccessible due to significant tool wear at the corresponding spindle (and cutting) speeds. In these cases, changing the teeth spacing can yield stable zones where they would not otherwise exist. Varying the helix angle from tooth to tooth has also been implemented to reduce chatter [44], but we will focus on variable teeth spacing here.

IN A NUTSHELL Because non-proportional tooth spacing disturbs regeneration of waviness, it can improve milling stability. Not all spacing selections increase stability, however, and whether or not there is improvement depends on the system dynamics, tooth spacing, and spindle speed. In addition, stability improvement by this technique generally requires an accompanying feed reduction. Constant spindle speed with non-proportional tooth spacing produces a non-constant feed per tooth. Because the maximum permissible chip load is a function of the cutting edge strength, the maximum feed for a tool with non-proportionally spaced teeth is controlled by the tooth with the largest preceding angle. All other teeth are essentially under used and the required feed reduction must be recovered through an increased axial depth of cut to simply break even in terms of the material removal rate.

6.7.1 Simulation Updating

As described in Section 4.3, there is a periodic time delay between teeth engagements due to the (typically) uniform teeth spacing. Changing the teeth spacing, therefore, varies this time delay and interrupts the surface regeneration periodicity. We can explore this through minor modifications to our time-domain simulations. First, let's consider the circular tool path code. The first modification is to directly define the angles of the individual teeth starting from tooth 1 located at an initial angle of zero. The teeth are ordered by increasing clockwise angles as described in Section 4.4 and shown in Fig. 6.3.1. Teeth angles of {0 95 180 275} deg are depicted, where teeth 2 and 4 have been advanced by five degrees relative to their uniform spacing angles of 90 degrees. To describe the teeth spacing, a new vector is defined in p_6_3_1_1.m.

```
tooth_angle = [0 95 180 275];
```

Due to the variable teeth angles, the feed per tooth also changes from one tooth to the next. This is handled using the following code, where `ft_mean` is the mean feed per tooth value (m/tooth) and `theta` is the angle between teeth (deg); it is defined using the MATLAB® `diff` function.

```
ft_mean = 0.15e-3;
theta = diff([tooth_angle 360]);
for cnt = 1:Nt
    ft(cnt) = (ft_mean*theta(cnt)*Nt)/360;
end
```

Based on these modifications, two additional changes are made. First, the `teeth` vector, which is used to index the appropriate `phi` entry, is redefined using the following `for` loop. The `round` function is necessary because the teeth entries must be integer values.

```
for cnt = 1:Nt
    teeth(cnt) = round(tooth_angle(cnt)/dphi) + 1;
end
```

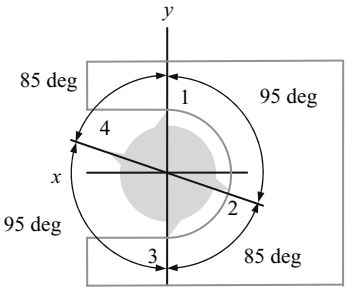

Fig. 6.3.1 Variable teeth spacing example with four teeth at angles {0 95 180 275} deg

Finally, each time the feed per tooth appears, it must now be indexed using the tooth (`Nt`) counter: `ft(cnt3)`. Note that the runout vector entries, `RO`, must now correspond to the appropriate entries in `tooth_angle`.

Example 6.3.1: Comparison of uniform and variable teeth spacing forces Let's compare the cutting forces produced by endmills with uniform and variable teeth spacing. We'll consider the same 30% radial immersion up milling cut (zero start angle and 66.4 deg exit angle) as in the previous section. Again, there are two identical modes in the x and y directions with modal parameters: $f_{n1} = 800$ Hz, $k_{q1} = 2 \times 10^7$ N/m, and $\zeta_{q1} = 0.05$; and $f_{n2} = 1000$ Hz, $k_{q2} = 1.5 \times 10^7$ N/m, and $\zeta_{q2} = 0.03$. The workpiece material is an aluminum alloy machined with a four tooth, 19 mm diameter square endmill using a feed per tooth of 0.15 mm/tooth. The cutting force coefficients are $k_t = 520$ N/mm^2 and $k_n = 300$ N/mm^2. We'll consider tools with zero helix angles (straight teeth) and tooth angles of {0 90 180 270} deg and {0 95 180 275} deg.

Figure 6.3.2 shows the resultant forces for an axial depth of 3 mm at 15000 rpm. The figure is produced using p_6_3_1_1.m, where the teeth numbers are marked according to the convention shown in Fig. 6.3.1. Both cuts are clearly stable; however, we see that the time between one tooth's exit and the next tooth's entry (where the force is zero) varies periodically with the variable teeth spacing. As we'd expect, the time is smaller for the decreased spacing between teeth 1 and 4 and, similarly, teeth 3 and 2.

Next let's explore the global stability behavior of the variable teeth spacing tool relative to the uniform teeth spacing tool. We obtain the stability lobe diagram for the latter using p_6_3_1_2.m; see Fig. 6.3.3. To establish a baseline for the comparison of the time-domain and frequency-domain solutions, let's

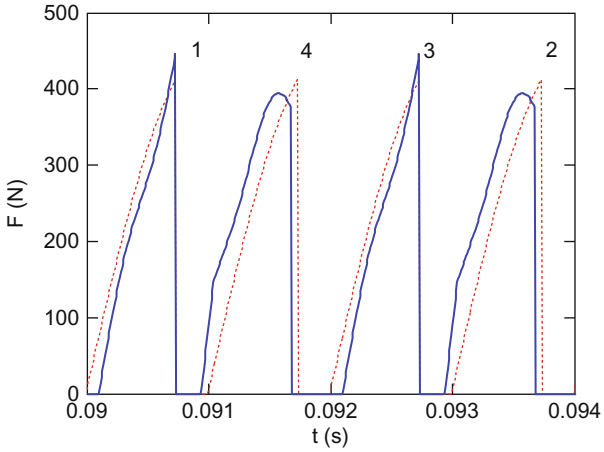

Fig. 6.3.2 Resultant cutting force for uniform (dotted line) and variable (solid line) teeth spacing with angles {0 95 180 275} deg. The helix angle is zero, the axial depth of cut is 3 mm, and the spindle speed is 15000 rpm for the 30% radial immersion up milling cut. The teeth numbers are also identified (as depicted in Fig. 6.3.1)

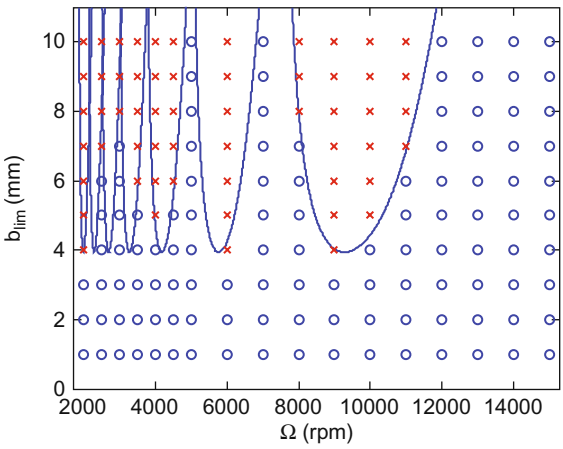

Fig. 6.3.3 Stability limits for uniform teeth spacing cutter. The frequency-domain solution for the same tool geometry is identified by the solid line. Using the circular tool path time-domain simulation, stable results are identified by circles and unstable results by 'x' symbols

select a grid of points and complete time-domain simulations using p_6_3_1_1.m. For each {Ω, *b*} combination, we determine stability from the corresponding force and displacement profiles. The stable cuts are marked with a circle in Fig. 6.3.3 and the unstable cuts with an 'x'. Good agreement is observed.

Implementing the variable teeth spacing {0 95 180 275} deg yields the results provided in Fig. 6.3.4. Again, the variable teeth spacing stability is compared to the frequency-domain uniform teeth spacing solution. A significant increase in the allowable axial depth of cut is observed in the region near 4000 rpm.

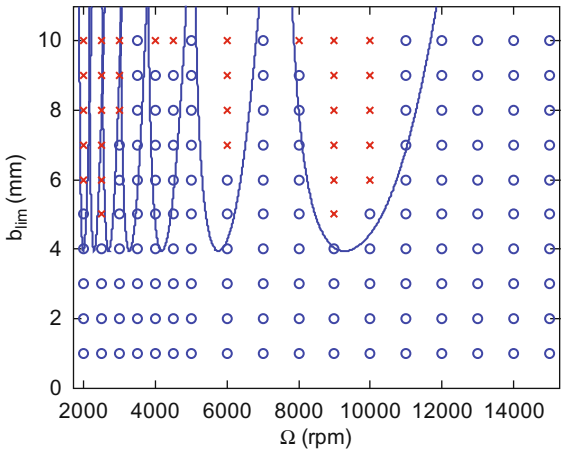

Fig. 6.3.4 Stability limits for variable teeth spacing, {0 95 180 275} deg, cutter. The frequency-domain solution for the uniform teeth spacing cutter is again identified by the solid line. Using the circular tool path time-domain simulation for the variable teeth spacing cutter, stable results are identified by circles and unstable results by 'x' symbols. Improved stability is seen near 4000 rpm

Although we would not expect the same behavior for different system dynamics, this example does demonstrate the potential gains made available by selection of appropriate tooth angles.

In a similar manner, we can model variable teeth spacing in the cycloidal tool path time-domain milling simulation by specifying the appropriate teeth angles in the vector `teeth`. This vector serves the same function as `tooth_angle` in the circular tool path simulation. See the MATLAB® program p_6_2_4_1.m included on the companion CD

6.4 Low Radial Immersion Milling

In 1998, Davies *et al.* reported that "undesirable vibrations observed in partial immersion cuts seem inconsistent with existing theory" [10]. Using a Poincaré sectioning technique (once-per-revolution sampling) combined with capacitive measurements of the tool shank displacements in the x (feed) and y directions during cutting, they found that some unstable low radial immersion cuts gave discrete clusters of once-per-revolution sampled points when plotted in the x-y plane, while others presented elliptical distributions. They subsequently showed that this behavior was the manifestation of two different types of instability [45–46]. Traditional quasiperiodic chatter, also referred to as Hopf bifurcation[2], leads to the elliptical distribution of periodically sampled points. The second instability type, encountered during low (less than 25%) radial immersions, is a period doubling, or flip, bifurcation. It reveals itself as two tightly grouped clusters of sampled points as opposed to a single group of points for the synchronous vibrations that occur during stable cutting with forced vibrations only. Subsequent modeling efforts are described in [47-53] and include temporal finite element analysis, time-domain simulation, a multi-frequency analytical solution, and the semi-discretization approach. These techniques give improved accuracy for the predicted stability limit over the average tooth angle and frequency-domain approaches (Chapter 4) in very low radial immersion (less than 10%) cases. However, they do not offer the convenient closed-form expressions for the stability boundary.

IN A NUTSHELL The cutting force in low radial immersion milling resembles a series of impacts. In between impacts, the tool experiences free vibration. The new cutting force depends on where the tool is in its decaying free vibration cycle when the tooth next encounters the previous surface. The result is the formation of additional stable areas near what was previously the worst case for stability.

[2] In the analysis of dynamic systems, a bifurcation represents the sudden appearance of a qualitatively different solution for a nonlinear system as some parameter is varied [61].

Example 6.4.1: Low radial immersion stability We can use time-domain simulation to explore the Hopf and flip bifurcations. By modifying the cycloidal tool path code to include once-per-revolution sampling, we can observe the two instabilities in x (feed direction) versus y displacement plots [10]. We'll use single degree of freedom, symmetric dynamics ($f_n = 720$ Hz, $k = 4.1 \times 10^5$ N/m, and $\zeta = 0.009$) for a 5% radial immersion up milling cut (zero start angle and 25.8 deg exit angle). The workpiece material is an aluminum alloy machined with a single tooth, 45 degree helix, 8 mm diameter square endmill using a feed per tooth of 0.1 mm/tooth. The cutting force coefficients are $k_t = 644$ N/mm^2 and $k_n = 238$ N/mm^2. These conditions mimic those reported in [53] to enable convenient comparison. The code added in p_6_4_1_1.m to enable once-per-revolution sampling follows, where `xpos` and `ypos` are the tool displacements in the x and y directions, respectively, `steps_rev` is the number of simulation steps per revolution of the cutter, and `xsample` and `ysample` are the sampling results.

```
xsample = xpos(1:steps_rev:length(xpos));
ysample = ypos(1:steps_rev:length(ypos));
```

Figure 6.4.1 shows the stability limit obtained using the frequency-domain solution (Section 4.3) as a solid line. The region shown corresponds to the left side of the $j = 0$ (rightmost) lobe. The results of time-domain simulations are identified by: circles (stable); 'x' symbols (Hopf bifurcation); and triangles (flip bifurcation). A narrow band of increased stability is seen between 27000 rpm and 28000 rpm. This is accompanied by the spindle speed range from 29000 rpm and 32000 rpm which exhibits flip bifurcation behavior. Three points are selected for further study. The {28000 rpm, 2 mm} point demonstrates the traditional Hopf instability; see Fig. 6.4.2 for the time history and Fig. 6.4.3

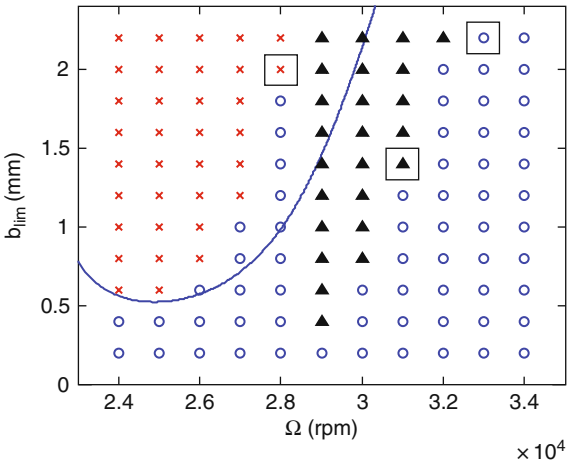

Fig. 6.4.1 The frequency-domain solution stability limit (solid line) is compared to time-domain simulation results for the $j = 0$ lobe. For the time-domain simulations, stable cuts are represented by circles and unstable cuts by 'x' symbols (Hopf) and triangles (flip)

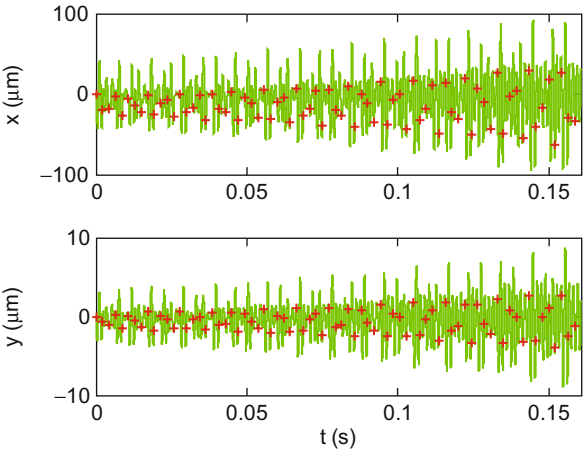

Fig. 6.4.2 Time history for the x (feed) and y direction displacements obtained from the {28000 rpm, 2 mm} cut in Fig. 6.4.1. The once-per-revolution sampled data ('+' symbols) demonstrate quasiperiodic, Hopf instability

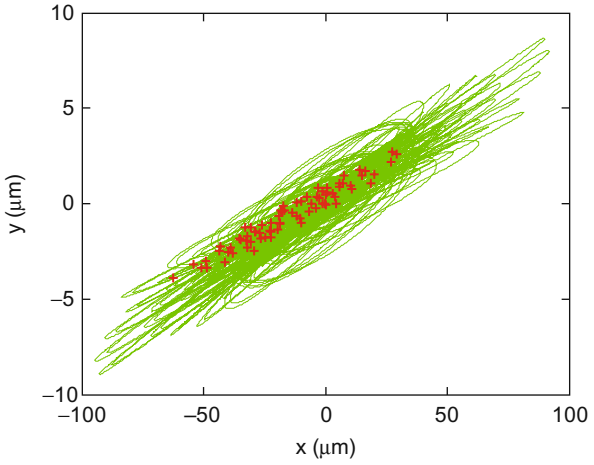

Fig. 6.4.3 Plot of x versus y direction displacements obtained from the {28000 rpm, 2 mm} cut. The elliptical distribution of the once-per-revolution sampled data ('+' symbols) indicates Hopf instability

for the x vs. y plot. As discussed previously, the once-per-revolution sampled data appears as an elliptical distribution for Hopf instability. Conversely, Figs. 6.4.4 and 6.4.5 show the flip bifurcation for the {31000 rpm, 1.4 mm} operating parameters. The synchronously sampled data now occur in two clusters after the initial transients attenuate in the x vs. y plot (Fig. 6.4.5). A stable cut is represented by the {33000 rpm, 2.2 mm} spindle speed, axial depth of cut pair. As expected, Figs. 6.4.6 and 6.4.7 display repetitive behavior from one revolution to the next (forced vibration only).

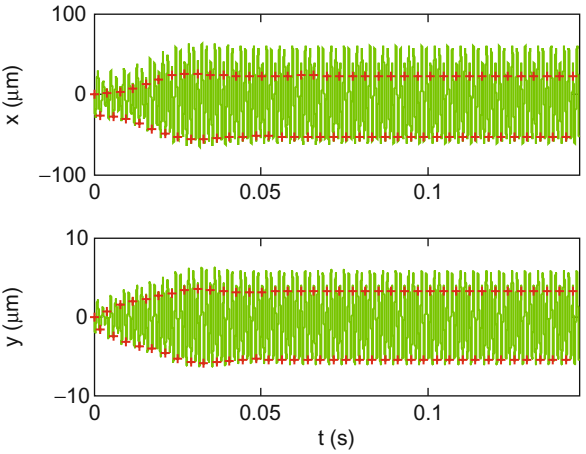

Fig. 6.4.4 Time history for the x (feed) and y direction displacements obtained from the {31000 rpm, 1.4 mm} cut. The once-per-revolution sampled data ('+' symbols) demonstrate a flip bifurcation

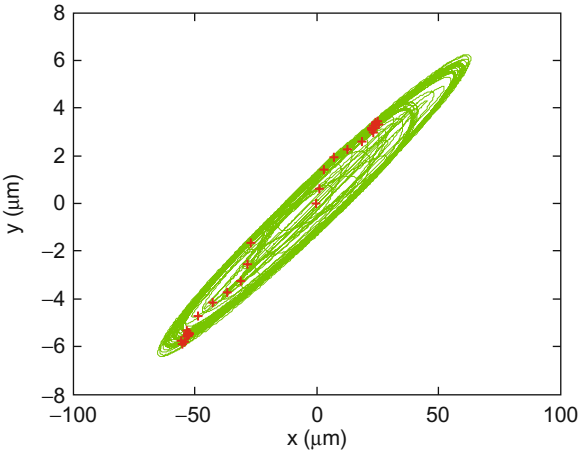

Fig. 6.4.5 Plot of x versus y direction displacements obtained from the {31000 rpm, 1.4 mm} cut. The two clusters of once-per-revolution sampled data ('+' symbols) identify a flip instability

IN A NUTSHELL For those concerned with detailed process modeling, the exact nature of the milling instability (Hopf or flip bifurcation) is extremely interesting. For practical machining applications, we just need to consider the radial depth of cut. As long as the radial depth is high, then the stability lobe algorithms described in Section 4.3 are valid. When the radial depth of cut is low, additional stable zones appear that "split" the higher radial depth stability lobes.

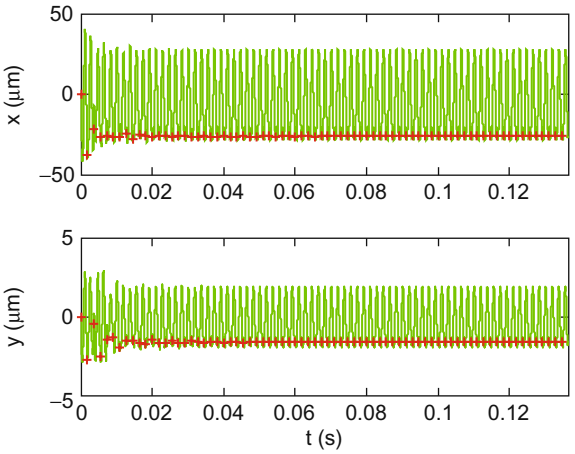

Fig. 6.4.6 Time history for the x (feed) and y direction displacements obtained from the {33000 rpm, 2.2 mm} cut. The once-per-revolution sampled data ('+' symbols) demonstrate stable behavior

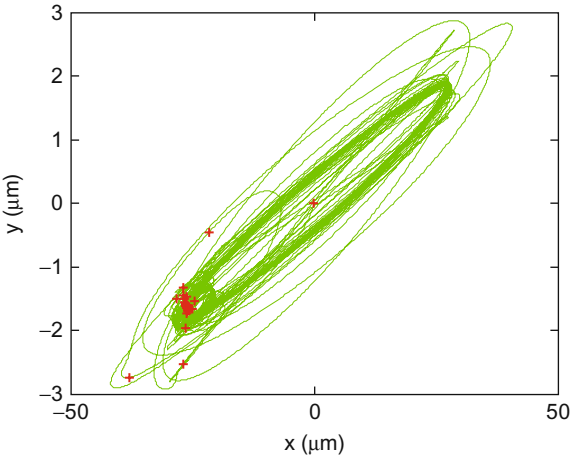

Fig. 6.4.7 Plot of x versus y direction displacements obtained from the {33000 rpm, 2.2 mm} cut. The single cluster of once-per-revolution sampled data ('+' symbols) indicates stable operation

6.5 Uncertainty Propagation

In the stability lobe diagrams we've displayed so far, the stability boundary has been represented by a single line. This indicates step-like behavior, where the cut is stable below the line and unstable above. If the inputs were perfectly known and the theory exactly captured the physical behavior, then this step behavior could be true (although in practice, even experienced machinists could disagree over whether a particular cut was stable or unstable near the stability limit). However, no measured quantity, such as the cutting force coefficients or tool point frequency response function, is perfectly known. Instead, there are

uncertainties associated with these inputs. Additionally, the stability algorithms incorporate approximations that limit their accuracy.

As stated in the National Institute of Standards and Technology Technical Note 1297 [54], "the result of a measurement is only an approximation or estimate of the value of the specific quantify in question, that is, the measurand, and thus the result is complete only when accompanied by a quantitative statement of its uncertainty". The inclusion of a defensible uncertainty statement enables the user to determine his/her confidence in the measurement and its usefulness in decision making. This concept can be extended to simulation results based on measured input quantities. Again, the user requires some indication of the reliability of the analysis output to gage its usefulness.

Guidelines for evaluating the uncertainty in measurement results are described in [54-57], for example. Often the measurand is not observed directly, but is expressed as a mathematical function of multiple input quantities. In this case, the fundamental steps in uncertainty estimation are to define the measurand, identify the input uncertainty contributors and their distributions, and propagate the uncertainties through the measurand using either analytical (Taylor series expansion) or sampling (such as Monte Carlo or Latin hypercube) approaches.

Identification of the uncertainty in the stability limit for both the average tooth angle [1] and frequency-domain [58] solutions is described in [59]. In this work, Monte Carlo simulation was applied to propagate uncertainties in the measured tool point FRF, cutting force coefficients (determined using the method outlined in Section 4.7), and radial depth of cut through the two approaches. In Monte Carlo simulation, random samples from the input variable distributions are selected and the output is computed over many iterations. The mean and standard deviation in the output are then reported. For the stability analyses, this requires that a new diagram is computed in each of the iterations. It is then necessary to identify the stability limit distribution at each spindle speed within the range of interest. The uncertainty is therefore spindle speed dependent and forms an envelope around the mean stability boundary as depicted in Fig. 6.5.1. To interpret the uncertainty region shown in the figure, we can state that it represents the axial depths, at the corresponding spindle speeds, where the cuts can either be stable or unstable. Above the upper bound,

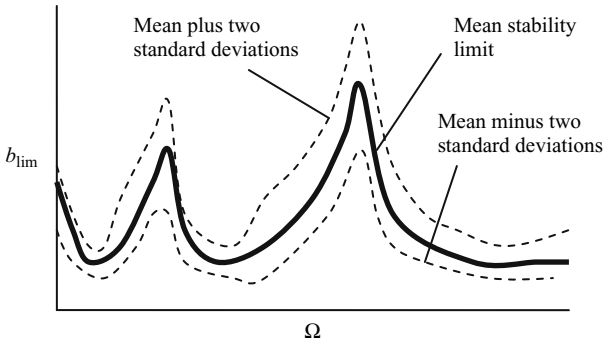

Fig. 6.5.1 Representation of two standard deviation uncertainty limits superimposed on the mean stability boundary determined from Monte Carlo simulation [59]

cuts are expected to be unstable, while cuts should be stable below the lower bound (with 95% confidence due to the selection of plus/minus two standard deviations about the mean). Naturally, we could apply the same approach to determining the uncertainty in surface location error predictions using the frequency-domain technique described in Section 5.2.

IN A NUTSHELL Uncertainties in the input data are part of the reason that simplified expressions for cutting forces and stability lobes are widely applied. It does not make much sense to attempt to model the location of the stability boundary with great accuracy when the force model coefficients, cutting geometry, system dynamics, etc. are only approximately known. Certainly there is an incentive (as in all of engineering) to strive for improved accuracy in models, but it is also sensible to avoid implementing models that are more complicated than the uncertainties in the required inputs warrant.

Exercises

1. For parts a) through d), indicate the action of an automatic spindle speed regulation system for chatter avoidance in milling. The chatter avoidance system operates by: 1) sampling the sound signal produced by the cutting process using a microphone; 2) computing the Fourier transform of the microphone signal; and 3) analyzing the spectrum content. Based on the spectrum content, a new spindle speed is recommended if chatter is sensed.
   a) The cutter has eight teeth, the spindle speed is 3000 rpm, and the frequency spectrum shows a large peak at 400 Hz. The maximum available spindle speed is 7500 rpm.
   b) The cutter has six teeth, the spindle speed is 4200 rpm, and the frequency spectrum shows a large peak at 380 Hz. The maximum available spindle speed is 5000 rpm.
   c) The cutter has four teeth, the spindle speed is 10000 rpm, and the frequency spectrum shows a large peak at 820 Hz. The maximum available spindle speed is 10000 rpm.
   d) The cutter has four teeth, the spindle speed is 30000 rpm, and the frequency spectrum shows a large peak at 1520 Hz. The maximum available spindle speed is 30000 rpm. The spindle speed is regulated once and the spectrum of the second cut shows a large peak at 2280 Hz.
2. Calculate the ε value(s) in radians which correspond to coincidence(s) between the runout harmonics and chatter frequencies for the $N = 0$ lobe when using a cutter with three teeth.
3. Chatter was observed for milling at 7000 rpm with a 4 mm axial depth of cut. The helical square end mill had four teeth. Using the diagrams provided in

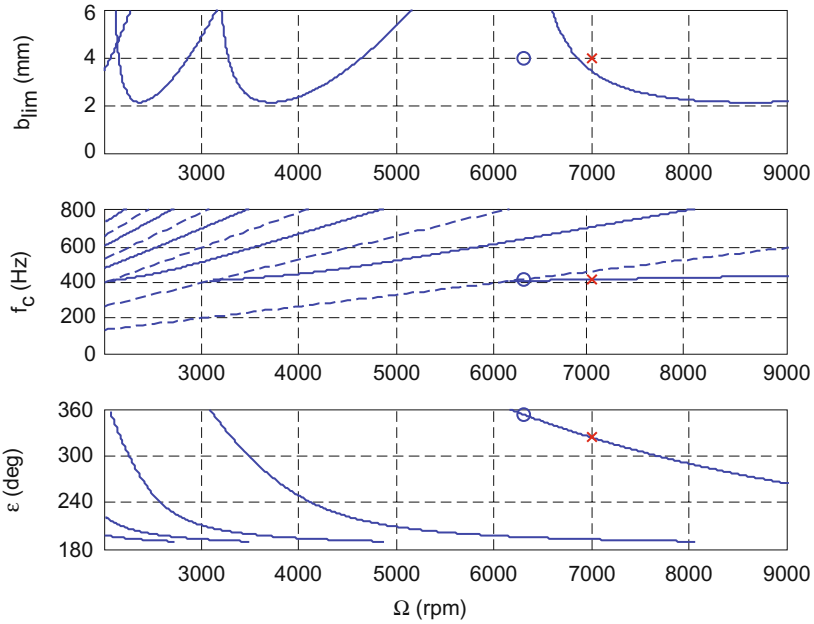

Fig. e.6.3 Stability, chatter frequency, and undulation phase diagrams

Fig. e.6.3, describe the automatic spindle speed regulation step(s) required to arrive at a stable cut. List the chatter frequency(s) encountered, the spindle speed(s) selected, and the corresponding ε value(s).

4. Consider a 30% radial immersion up milling cut. The tool dynamics are described by two identical modes in both the x and y directions (assume the workpiece is rigid). The modal parameters are: $f_{n1} = 800$ Hz, $k_{q1} = 2 \times 10^7$ N/m, and $\zeta_{q1} = 0.05$; and $f_{n2} = 1000$ Hz, $k_{q2} = 1.5 \times 10^7$ N/m, and $\zeta_{q2} = 0.03$. The workpiece material is an aluminum alloy and it is machined with a four tooth, 12.7 mm diameter, 30 deg helix square endmill using a feed per tooth of 0.2 mm/tooth. The variable teeth spacing for this cutter is `teeth= [ 0 95 180 275]` deg. The cutting force coefficients are $k_t = 520$ N/mm^2, $k_n = 300$ N/mm^2, and $k_{te} = k_{ne} = 0$. The axial depth of cut is 5 mm and the spindle speed is 15000 rpm. Determine the roughness average (in μm) for runout values of `RO=[ 0 0 -20 0]` μm using the cycloidal tool path time-domain simulation. Compare this value to the roughness average with zero runout.

References

1. Tlusty, J., W. Zaton, and F. Ismail, 1983, Stability Lobes in Milling, Annals of the CIRP, 32/1: 309–313.
2. Smith, S. and Tlusty, J., 1992, Stabilizing Chatter by Automatic Spindle Speed Regulation, Annals of the CIRP, 41/1: 433–436.

3. Delio, T., Tlusty, J., and Smith, S., 1992, Use of Audio Signals for Chatter Detection and Control, Journal of Engineering for Industry, 114: 146–157.
4. Smith, D., Smith, S., and Tlusty, J., 1998, High Performance Milling Torque Sensor, Journal of Manufacturing Science and Engineering, 120/3: 504–514.
5. Smith, S. and Delio, T., 1992, Sensor-based Chatter Detection and Avoidance by Spindle Speed Selection, Journal of Dynamic Systems, Measurement, and Control, 114/3: 486–492.
6. Schmitz, T., Davies, M., Medicus, K., Snyder, J., 2001, Improving High-Speed Machining Material Removal Rates by Rapid Dynamic Analysis, Annals of the CIRP, 50/1: 263–268.
7. Schmitz, T., Medicus, K., and Dutterer, B., 2002, Exploring Once-per-revolution Audio Signal Variance as a Chatter Indicator, Machining Science and Technology, 6/2: 215–233.
8. Schmitz, T., 2003, Chatter Recognition by a Statistical Evaluation of the Synchronously Sampled Audio Signal, Journal of Sound and Vibration, 262/3: 721–730.
9. Cheng, C.-H., Duncan, G.S., and Schmitz, T., 2007, Rotating Tool Point Frequency Response Prediction using RCSA, Machining Science and Technology, 11/3: 433–446.
10. Davies, M., Dutterer, B., Pratt, J., and Schaut, A., 1998, On the Dynamics of High-Speed Milling with Long, Slender Endmills, Annals of the CIRP 47/1: 55–60.
11. Tlusty, J., 1959, Systems and Methods of Machine Tool Testing, Microtechnic, 13: 162–178.
12. Bryan, J., Clouser, R., and Holland, B., 1967, Spindle Accuracy, American Machinist, 149–64.
13. American National Standards Institute, American Society of Mechanical Engineers, 1985, ANSI/ASME B89.3.4 M, Axes of Rotation: Methods for Specifying and Testing, New York.
14. Smith, S. and Winfough, W.R., 1994, The Effect of Runout Filtering on the Identification of Chatter in the Audio spectrum of Milling, Transactions of the NAMRI/SME, 22: 173–178.
15. Schmitz, T., Couey, J., Marsh, E., Mauntler, N., and Hughes, D., 2007, Runout Effects in Milling: Surface finish, Surface Location Error, and Stability, International Journal of Machine Tools and Manufacture, 47: 841–851.
16. Kline, W. and DeVor, R., 1983, The Effect of Runout on Cutting Geometry and Forces in End Milling, International Journal of Machine Tool Design and Research, 23/2-3: 123–140.
17. Armarego, E. and Deshpande, N., 1991, Computerized End Milling Force Predictions with Cutting Models Allowing Eccentricity and Cutter Deflections, Annals of the CIRP, 40/1: 25–29.
18. Altintas, Y. and Chan, P., 1992, In-Process Detection and Suppression of Chatter in Milling, International Journal of Machine Tools and Manufacture, 32/3: 329–47.
19. Liang, S. and Wang, J., 1994, Milling Force Convolution Modeling for Identification of Cutter Axis Offset, International Journal of Machine Tools and Manufacture, 34/8: 1177–1190.
20. Feng, H.-Y. and Menq, C.-H., 1994, The Prediction of Cutting Forces in the Ball-End Milling Process – I. Model Formulation and Model Building Procedure, International Journal of Machine Tools and Manufacture, 34/5: 697–710.
21. Feng, H.-Y. and Menq, C.-H., 1994, The Prediction of Cutting Forces in the Ball-End Milling Process – II. Cut Geometry Analysis and Model Verification, International Journal of Machine Tools and Manufacture, 34/5: 711–719.
22. Yan, D., El-Wardany, T., and Elbestawi, M., 1995, A Multi-Sensor Strategy for Tool Failure Detection in Milling, International Journal of Machine Tools and Manufacture, 35/3: 383–398.
23. Stevens, A. and Liang, S., 1995, Runout Rejection in End Milling through Two-Dimensional Repetitive Force Control, Mechatronics, 5/1: 1–13.
24. Hekman, K. and Liang, S., 1997, In-Process Monitoring of End Milling Cutter Runout, Mechatronics, 7/1: 1–10.

25. Baek, D., Ko, T., and Kim, H., 1997, A Dynamic Surface Roughness Model for Face Milling, Precision Engineering, 20/3: 171–178.
26. Zheng, H., Li, X., Wong, Y., and Nee, A., 1999, Theoretical Modeling and Simulation of Cutting Forces in Face Milling with Cutter Runout, International Journal of Machine Tools and Manufacture, 39/12: 2003–2018.
27. Yun, W.-S. and Cho, D.-W., 2001, Accurate 3-D Cutting Force Prediction using Cutting Condition Independent Coefficients in End Milling, International Journal of Machine Tools and Manufacture, 41/4: 463–478.
28. Baek, D., Ko, T., and Kim, H., 2001, Optimization of Feedrate in a Face Milling Operation using a Surface Roughness Model, International Journal of Machine Tools and Manufacture, 41/3: 451–462.
29. Mezentsev, O., Zhu, R., DeVor, R., Kapoor S., and Kline, W., 2002, Use of Radial Forces for Fault Detection in Tapping, International Journal of Machine Tools and Manufacture, 42/4: 479–488.
30. Ko, J., Yun, W.-S., Cho, D.-W., and Ehmann, K.F., 2002, Development of a Virtual Machining System, Part 1: Approximation of the Size Effect for Cutting Force Prediction, International Journal of Machine Tools and Manufacture, 42/15: 1595–1605.
31. Ranganath, S. and Sutherland, J., 2002, An Improved Method for Cutter Runout Modeling in the Peripheral Milling Process, Machining Science and Technology, 6/1: 1–20.
32. Wang, J.-J. and Zheng, C., 2003, Identification of Cutter Offset in End Milling without a Prior Knowledge of Cutting Coefficients, International Journal of Machine Tools and Manufacture, 43/7: 687–697.
33. Lazoglu, I., 2003, Sculpture Surface Machining: A Generalized Model of Ball-End Milling Force System, International Journal of Machine Tools and Manufacture, 43/5: 453–462.
34. Atabey, F., Lazoglu, I., and Altintas, Y., 2003, Mechanics of Boring Processes – Part II. Multi-Insert Boring Heads, International Journal of Machine Tools and Manufacture, 43/5: 477–484.
35. Slavicek, J., 1965, The effect of Irregular Tooth Pitch on Stability of Milling, Proceedings of the 6th Machine Tool Design and Research Conference, Pergamon Press, London, pp. 15–22.
36. Vanherck, P., 1967, Increasing Milling Machine Productivity by Use of Cutter with Non-Constant Edge Pitch, Proceedings of the 8th Machine Tool Design and Research Conference, pp. 947–960.
37. Doolan, P., Phadke, M.S., and Wu, S., 1975, Computer Design of Vibration Free Face Milling Cutters, Journal of Engineering for Industry, 97B/3: 925–930.
38. Doolan, P., Burney, F., and Wu, S., 1976, Computer Design of a Multi-purpose Minimum Vibration Face Milling Cutter, International Journal of Machine Tool Design and Research, 16/3: 187–192.
39. Tlusty, J., Ismail, F., and Zaton W., 1983, Use of Special Milling Cutters Against Chatter, Transactions of the NAMRI/SME, 11: 408–415.
40. Shirase, K. and Altintas, Y., 1995, Cutting Force and Dimensional Surface Error Generation in Peripheral Milling with Variable Pitch Helical End Mills, International Journal of Machine Tools and Manufacture, 36/5: 567–584.
41. Choudhurya, S. and Mathew, J., 1995, Investigations of the Effect of Non-uniform Insert Pitch on Vibration during Face Milling, International Journal of Machine Tools and Manufacture, 35/10: 1435–1444.
42. Altintas, Y, Engin, S., and Budak, E., 1999, Analytical Stability Prediction and Design of Variable Pitch Cutters, Journal of Manufacturing Science and Engineering, 121: 173–178.
43. Budak, E., 2003, An Analytical Design Method for Milling Cutters with Nonconstant Pitch to Increase Stability, Part 1: Theory, Part 2: Application, Journal of Manufacturing Science and Engineering, 123: 29–38.

44. Stone, B., 1970, The Effect on the Chatter Behavior of Cutters With Different Helix Angles on Adjacent Teeth, Proceedings of the 11th International Machine Tool Design and Research Conference, pp. 169–180.
45. Davies, M., Pratt, J., Dutterer, B., and Burns, T., 2000, The Stability of Low Radial Immersion Milling, Annals of the CIRP 49/1: 37–40.
46. Davies, M., Pratt, J., Dutterer, B., and Burns, T., 2002, Stability Prediction for Low Radial Immersion Milling, Journal of Manufacturing Science and Engineering, 124/2: 217–225.
47. Insperger, T., Mann, B., Stépàn, G., and Bayly, P., 2003, Stability of Up-milling and Down-milling, Part 1: Alternative Analytical Methods, International Journal of Machine Tools and Manufacture, 43/1: 25–34.
48. Mann, B., Insperger, T., Bayly, P., and Stépàn, G., 2003, Stability of Up-milling and Down-milling, Part 2: Experimental Verification, International Journal of Machine Tools and Manufacture, 43/1: 35–40.
49. Campomanes, M. and Altintas, Y., 2003, An Improved Time Domain Simulation for Dynamic Milling at Small Radial Immersions, Journal of Manufacturing Science and Engineering, 125/3: 416–422.
50. Merdol, S. and Altintas, Y., 2004, Multi Frequency Solution of Chatter Stability for Low Immersion Milling, Journal of Manufacturing Science and Engineering, 126/3: 459–466.
51. Bayly, P., Halley, J., Mann, B., and Davies, M., 2004, Stability of Interrupted Cutting by Temporal Finite Element Analysis, Journal of Manufacturing Science and Engineering, 125/2: 220–225.
52. Mann, B., Bayly, P, Davies, M., and Halley, J., 2004, Limit Cycles, Bifurcations, and Accuracy of the Milling Process, Journal of Sound and Vibration, 277/1-2: 31–48.
53. Govekar, E., Gradišek, J., Kalveram, M., Insperger, T., Weinert, K., Stépàn, G., and Grabec, I., 2005, On Stability and Dynamics of Milling at Small Radial Immersion, Annals of the CIRP, 54/1: 357–362.
54. Taylor, B. and Kuyatt, C., 1994, Guidelines for Evaluating and Expressing the Uncertainty of NIST Measurement Results, NIST Technical Note 1297 1994 Edition.
55. International Standards Organization (ISO), 1993, Guide to the Expression of Uncertainty in Measurement (Corrected and Reprinted 1995).
56. American National Standards Institute, 1997, ANSI/NCSL Z540-2-1997, US Guide to the Expression of Uncertainty in Measurement.
57. Bevington, P. and Robinson, D., 1992, Data Reduction and Error Analysis for the Physical Sciences, 2nd Edition, WCB/McGraw-Hill, Boston, MA.
58. Altintas, Y. and Budak, E., 1995, Analytical Prediction of Stability Lobes in Milling, Annals of the CIRP, 44/1: 357–362.
59. Duncan, G.S., Kurdi, M., Schmitz, T., and Snyder, J., 2006, Uncertainty Propagation for Selected Analytical Milling Stability Limit Analyses, Transactions of the NAMRI/SME, 34: 17–24.
60. Weisstein, E., "Incommensurate" from MathWorld – A Wolfram Web Resource, http://mathworld.wolfram.com/Incommensurate.html, accessed May, 2008.
61. Weisstein, E., "Bifurcation" from MathWorld – A Wolfram Web Resource, http://mathworld.wolfram.com/Bifurcation.html, accessed May, 2008.